Jet, Wave, and Droplet Velocities for a Continuous Fluid Jet*

Randy Fagerquist

Scitex Digital Printing, Inc., Dayton, Ohio 45420

This paper presents data showing the relationship of the jet velocity V_j, the wave velocity $V_w = \lambda f$, and the droplet velocity V_d of a continuous, stimulated jet emanating from an orifice in a thin, flat plate. The jet velocity measurement is nontrivially derived from the flow rate, as the jet diameter D is a function of V_j due to the presence of a dynamical meniscus at the orifice-jet boundary; λ is the measured wavelength of the surface deformation imposed on the jet at a frequency, f. The droplet velocity is measured in a straightforward fashion. We find good agreement between the measured values for λf and those calculated from the simple velocity potential theory for cylindrical jets for $\lambda/D < \pi$. However, the same theory predicts $\lambda f = V_j$ and $V_j > V_d$ for $\lambda / D > \pi$, which we do not find to be strictly true. A possible factor for this discrepancy is that the surface deformation along the length of the stimulated jet is monotonically increasing in amplitude, culminating in droplet formation and break-off. This finding strongly violates the assumption of a uniform and infinitesimal deformation in the simple theory.

Journal of Imaging Science and Technology 40: 405–411 (1996)

Introduction

The physics of liquid jet surface deformations is of great interest in the continuous ink-jet field due to the fundamental role it plays in determining droplet generation for the printing process. One of the questions that has become of some interest to us is how the large-amplitude deformations behave in comparison with the more well-known and understood small-amplitude deformations.

Rayleigh,[1] of course, addressed the basic problem of the infinite liquid cylinder with an imposed uniform surface perturbation. He was able to show many of the salient features of the jet deformation growth as a function of time. In reality, however, the liquid jets used for our ink-jet printing do not have infinite extent and do not usually have small perturbations at the surface. The jets, in a properly operating printer, have a relatively short length before breaking up into droplets. This is accomplished by imposing a substantial surface deformation on the jet as it exits the orifice.

A large part of our investigation includes the measurement of three velocities associated with the break-up of the jets: the average jet velocity as it exits the nozzle, the velocity of the droplets after the jets break-up, and the wave velocity of the surface deformations propagating on the surface of a stimulated jet.

Original manuscript received March 18, 1996.

* Presented in part at IS&Ts 11th International Congress on Advances in Non-Impact Printing Technologies, October 29–November 3, 1995, Hilton Head, South Carolina.

Jet Velocity. In principle, the velocity of an unstimulated jet is easily determined from the flow rate, Q, and the jet diameter, D, by:

$$V_j = \frac{4Q}{\rho \pi D^2}. \quad (1)$$

We found in previous experiments[2] that the jet diameter was not equal to the orifice diameter, due to fluid wetting of the surface of the nozzle plate around the nozzle. The difference between jet diameter and orifice diameter can lead to substantial errors in the calculation of V_j from Eq. 1. If one assumes that the value of D is the same as the orifice diameter, and if D, ρ, and Q are measured with an accuracy of, say, 1%, then the error for V_j is on the order of 4%. The error in Eq. 1 enters as $2\Delta D$ and makes necessary an independent measurement of D for the range of jet velocities investigated here.

Droplet Velocity. The droplets that form from the breakup of the jets travel with a velocity parallel to the jet velocity. A typical video image of an array of droplets in flight used for measuring droplet spacing, L, is shown in Fig. 1. The magnitude of the droplet velocity was measured by using a stroboscopic light source backlighting the array of droplets after breakoff so that they appear fixed in space. A microscope with reticule or a video image of the array can be used to determine the spacing of the droplets in the direction of travel. Knowing the frequency of jet stimulation, f_s, allows the droplet velocity, V_d, to be calculated from

$$V_d = f_s \cdot L, \quad (2)$$

where L is the droplet spacing in the direction of the velocity. An artifact of the droplet breakoff process is visible in the figure as a periodic distortion of the droplets from perfect spherical shapes. The droplets in the row near the center of the figure are somewhat flattened on the top and bottom, compared with those in the row just above or below it. The first and last two rows show droplets that are elongated in the direction of V_d. This is typical of the oscillating droplet geometry that is observed immediately below the breakoff point. Even though the droplet shape is oscillating, the velocity of the center of the droplet mass is constant.

Wave Velocity. ***Small-Amplitude Waves***. The most interesting of the three velocities studied here is the wave velocity. Rayleigh[1] found that there were two regimes for periodic surface deformations on the ideal infinite cylinder of fluid. The first regime is defined by $\lambda/D < \pi$, where λ is the wavelength of the disturbance. The amplitude of the surface deformations in this regime decreases with time because of viscosity effects on the wave propagation and surface energy minimization (see Fig. 2).

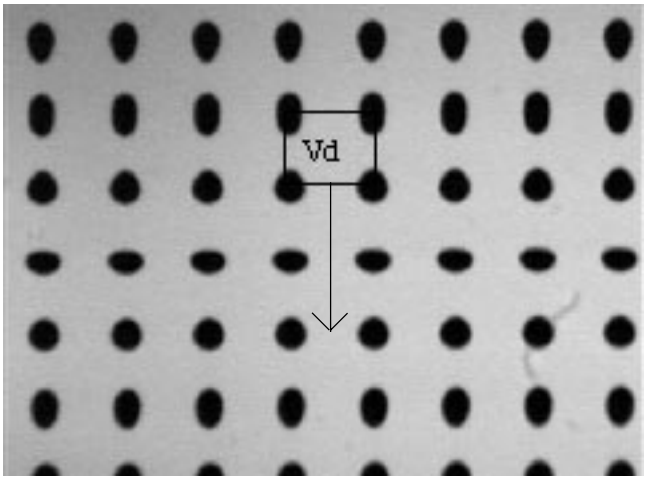

Figure 1. Video image of droplets in flight after breakoff.

Figure 2. Stimulated jets with $\lambda/D < \pi$.

The simplest form of the problem of an infinite jet with surface deformations is given by the following:

1. The fluid is considered nonviscid.
2. The flow is nonrotational: $\nabla \times \mathbf{V} = \nabla \cdot \boldsymbol{V} = 0$.
3. The fluid density ρ = constant.
4. $\frac{1}{2}\rho V^2$ in Bernoulli's equation is negligible compared with the other terms.
5. The velocity potential, ϕ, is defined by

$$-\frac{\partial \phi}{\partial r} = \mathbf{V}_r, -\frac{\partial \phi}{\partial z} = \mathbf{V}_z, \nabla \phi = \mathbf{V}$$

The differential equation for this problem is the cylindrical Laplacian:

$$\frac{\partial^2 \phi}{\partial r^2} + \frac{1}{r}\frac{\partial \phi}{\partial r} + \frac{\partial^2 \phi}{\partial z^2} = 0. \tag{3}$$

A product solution of the form $\phi = R(r)Z(z)T(t)$ is assumed, and the boundary condition at the surface of the jet is approximated by

$$V_r(R) = \frac{dR}{dt} = -\frac{\partial \phi}{\partial r} \text{ at } r = R; \quad \text{and } \frac{\partial R}{\partial z} << 1,$$

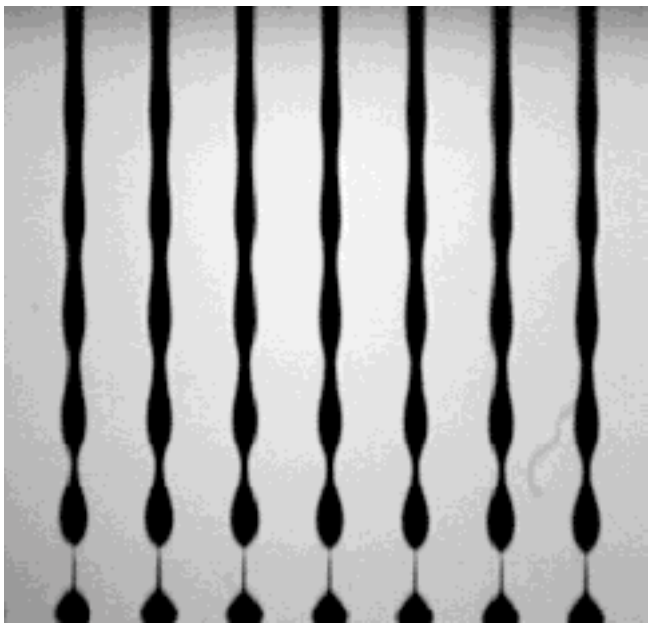

Figure 3. Stimulated jets with $\lambda/D > \pi$.

so that the curvature at the surface of the jet can be simplified to

$$\frac{\partial^2 R}{\partial z^2} \approx \frac{\frac{\partial^2 R}{\partial z^2}}{\left[1 + \left(\frac{\partial R}{\partial z}\right)^2\right]^{3/2}}.$$

These approximations, conditions, and restrictions then allow a simple harmonic solution to Eq. 3, which yields the dispersion relation:

$$\omega^2 = \left[\left(k^2 r_0^2 - 1\right)\left(\frac{k}{r_0^2}\right)\frac{I_1(kr_0)}{I_0(kr_0)}\right]\frac{\sigma}{\rho}, \tag{4}$$

where σ = surface tension of the fluid, ρ = fluid density, r_0 = unperturbed jet radius, $k = 2\pi/\lambda$, $\omega = 2\pi f$, and $I_0(kr_0)$ and $I_1(kr_0)$ are Bessel functions. The dispersion relation shows that for $kr_0 > 1$ ($\lambda/D < \pi$), ω is real and positive and represents the angular frequency of a wave on the surface of the jet propagating with the phase velocity, $V_p = \omega/k$. [Note that Eq. 4 yields the right dispersion relation for propagating plane waves on the surface of a level liquid by taking the limits $k \to \infty$ (short wavelength) or $r_0 \to \infty$ (large radius)].

Large-Amplitude Waves. The second regime is determined by the condition $kr_0 < 1$ ($\lambda/D > \pi$), and shows remarkably different behavior from the disturbances discussed above. Here ω is imaginary and describes the case where the amplitude of the disturbance grows as a function of time at an exponential rate, but is at rest with respect to the fluid, according to the simple theory. That is, the disturbance is assumed to grow in amplitude without propagating along the length of the jet. The amplitude of the perturbed surface increases until it reaches the value of the jet radius. At this point, the continuous jet of fluid breaks up into equal mass drops.

When the amplitude of the disturbance on the jet is no longer small enough to satisfy the boundary conditions and approximations discussed above, then the solutions

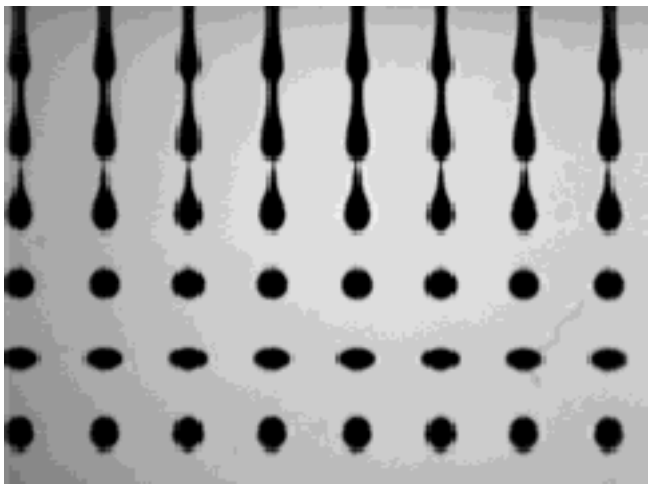

Figure 4. Large-amplitude initial disturbance.

to Eq. 3 are less likely to describe properly the wave motion or disturbance amplitude growth that takes place. A large-amplitude disturbance can be obtained by allowing a true perturbation to grow until the surface variation is on the order of the jet radius, as in Fig. 3, or by a large initial deformation, as shown by Fig. 4.

Experimental

Our experimental work was carried out with printhead components from the Scitex 5100 printer. The droplet generators had 132 jets formed by forcing fluid through orifices in a thin nickel plate, with orifice diameters ranging from 1.86 to 1.88 mils. The printhead test stand was equipped to provide wide-range frequency stimulation of the jets and variable fluid pressure. A proprietary liquid ink with well-known fluid properties was used as the test fluid.

An LED strobe light source, a microscope and reticule, and a Mideo Systems video imaging system with Media Cybernetics ImagePro Plus analysis software were used to record the jet surface deformations and free droplet positions during the course of the experiment. Data analysis, preparation, and presentation were accomplished with ImagePro, MS Excel, and MS Word software.

Jet Velocity. The average flow rate, Q, of a jet at each test pressure was measured by collecting the jetted fluid of 132 individual jets for a known amount of time and weighing the fluid. The fluid pressure was electromechanically controlled to better than ±0.05 psi. This procedure was performed several times for each condition, so that an average value of the flow rate was obtained.

The density of the fluid used for these experiments was determined at the time of manufacture and was checked periodically during the experiments. The fluid supply was also routinely replaced during the course of the experimentation, so that any variations of the data due to fluid density fluctuations could be kept minimal.

Measurements of D versus the fluid pressure, P, were made using two different setups. The first method employed a strobe light source backlighting the unstimulated jet array and a photodetector in conjunction with a microscope focus on a portion of the jet array. The jets were imaged onto the photodetector, which was connected to a lock-in amplifier referenced to the strobe source. When the pressure of the fluid behind the orifice plate was varied, the diameters of the jets changed in concert with the jet velocity, causing the "shadow" cast by the jets on the detector to vary in proportion to the changing diameters. This caused the output of the detector to vary accordingly; the output was then amplified with a high signal-to-noise ratio by the lock-in amplifier. The output voltage of the lock-in amplifier was, in this setup, proportional to the average diameter of the jets in view of the microscope.

The lock-in measurement had the advantage of having very high resolution, with the detector output being an analog signal proportional to the amount of light striking it. This method had the disadvantage of being difficult to calibrate and sensitive to detector and light source drift. It also was generally used with low-power microscope magnification of the jets, and therefore the results are values of D that are averages over several individual jets.

The second method of jet diameter measurement was direct analysis of the video images of highly magnified, unstimulated jets, made with the Mideo Systems video system. Many individual measurements of several jets for each trial were made and averaged, producing an average diameter for a single jet.

Because the jet images were made with the video system having two jets always in the field of view, and because the jet spacing for the arrays used were very well known, these images were self-calibrating. This proved to be a big advantage over the lock-in method, where absolute calibration was difficult to achieve. The major disadvantage of the video method was that, because the captured images were digital, the resolution of the D measurements was often lower than that provided by the lock-in method. This was partially compensated for by using many images and measurements and finding an average value for a jet diameter.

Drop Velocity. An extensive series of measurements was made, using the video imaging of the droplet positions to obtain values for V_d. These measurements were made for 3.0- and 9.5-psi fluid pressures. The 9.5-psi trials were repeated for stimulation frequencies of 32.663, 48.778, and 67.113 kHz. The 3.0-psi trial used a stimulation frequency of 24.442 kHz.

Video images like the one shown in Fig. 1 were analyzed with an image analysis program. This program had several advanced features, including one that determined the position of the droplet centroids in the x and y directions. The difference between neighboring droplet centroids in the velocity direction is L, from which V_d can be determined, using Eq. 2.

Some care was given to making the droplet velocity measurements reasonably close to the point of breakoff, so that aerodynamic drag did not slow the droplets enough to produce an error in the measurement of L. However, if the measurements are attempted too close to the breakoff point, the position of the droplet center of mass becomes more difficult to determine because of the large distortion of the droplet shape, as previously mentioned. Generally, the droplet position measurements were made on an array of droplets a few λ below the breakoff point to minimize the effects of both air drag and distorted droplet geometry.

Wave Velocity. Images similar to those shown in Fig. 2 (propagation mode) and Fig. 3 (amplitude growth mode) were also recorded with the video measurement system. The images were analyzed with the Image Pro software, giving the jet radius, r, as a function of the distance along the axis of the jet, z. The wavelength, λ, of the surface deformations was obtained by measuring the distance along z between the maxima (or minima) in the figure. The wave velocity, V_w, was then determined from Eq. 2 using the known frequency of jet stimulation, f, and the measured wavelength, λ.

TABLE I.

Pressure (psi)	Stimulaton Freq. (kHz)	Q (10^{-6} kg/s)	D (10^{-5} m)	λ/D	V_w (m/s)	V_d (m/s)	V_j (m/s)
3.0	24.442	9.130 ± 0.003	5.28 ± 0.05	3.3	4.20 ± 0.07	3.78 ± 0.03	4.12 ± 0.05
9.5	32.663	16.90 ± 0.03	4.79 ± 0.10	6.1	9.48 ± 0.04	9.10 ± 0.02	9.21 ± 0.23
9.5	48.778	16.90 ± 0.03	4.79 ± 0.10	4.1	9.55 ± 0.08	9.22 ± 0.02	9.21 ± 0.23
9.5	67.133	16.90 ± 0.03	4.79 ± 0.10	3.0	9.57 ± 0.06	9.25 ± 0.02	9.21 ± 0.23

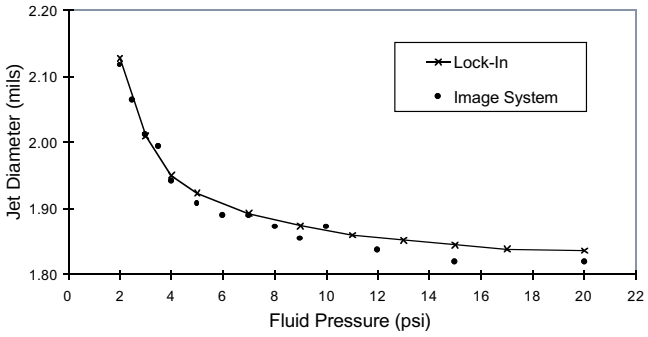

Figure 5. Average single jet diameter versus pressure.

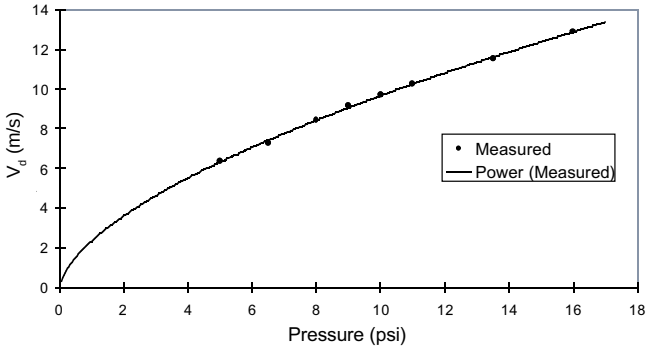

Figure 6. Droplet velocity versus pressure.

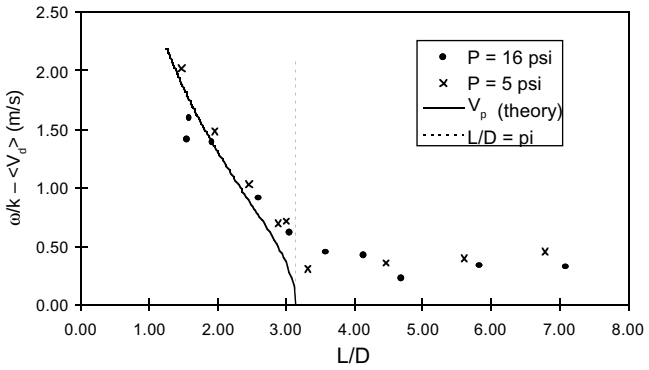

Figure 7. Plot of $\omega/k - \langle V_d \rangle$ versus λ/D.

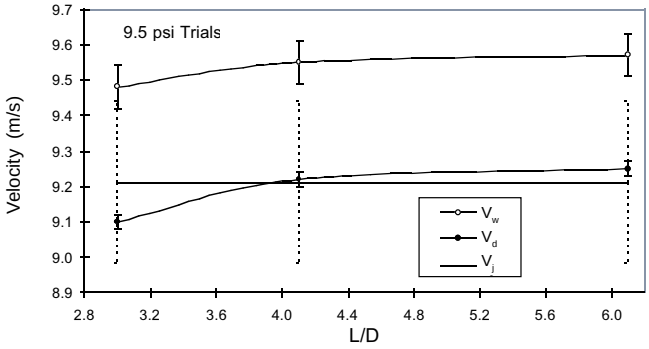

Figure 8. The velocities V_w, V_d, and V_j versus λ/D for 9.5 psi.

Results

Jet Velocity. The dependence of D on P is shown in Fig. 5, which includes measurements of D by both the video and lock-in methods. As can be seen, the diameter of the jet is found to increase rapidly as P decreases toward 0 psi. As the pressure increases, the jet diameter decreases and appears to approach an asymptotic lower limit at higher pressures. With Q, D, and ρ being known (measured) quantities, the values for V_j were calculated from Eq. 1. The results of our measurements of jet velocity at 3.0 and 9.5 psi are given in Table I.

Drop Velocity. Measured values for the droplet velocity at 3.0 and 9.5 psi are also shown in Table I. Additional data are shown in Fig. 6, where V_d is plotted as a function of P. The solid line in the figure is a power law fit of the data to $V_d = a(P - P_0)^x$, where P_0, a, and x are fitted parameters. The values of the fitted parameters are $P_0 = 0.05$ psi, $x = 0.61$, and $a = 2.4$, where the units for a are consistent with P raised to the x power.

The values for x and P in simple Bernoulli theory are 0.5 and 0 psi, respectively. The deviations of x and P_0 from these values are probably the result of viscosity effects and the possibility that the droplet velocity is slightly retarded upon breaking off from the jet because of surface tension effects (which are discussed later). The deviations from Bernoulli theory are relatively small, though, and not important here, because only the measured values of the droplet velocity are of interest.

Wave Velocity. Measurements of the wave velocity, $V_w = \omega/k$, and the droplet velocity, V_d, at $P = 5$ and 16 psi were made at a number of values of λ/D. The difference between V_w and V_d, which is the velocity of the wave on the jet in the frame of reference where the dropets are stationary, is calculated and plotted in Fig. 7. The solid line to the left of $\lambda/D = \pi$ is the phase velocity, V_p, calculated from the dispersion relation, Eq. 4, with the proper parameters for the test conditions used. As can be seen in the figure, the theoretical calculations for ω/k (in the frame of reference where the jet is staionary) are very close to the measured values of $V_w - V_d$. To the right of $\lambda/D = \pi$, the value of V_p is approximately constant and slightly larger than zero. This is possibly due to droplet slowing at breakoff ($V_j > V_d$) or the wave on the jet surface having a small velocity relative to the jet that is weakly dependent on, or even independent of, the stimulation frequency.

Figure 8 is a plot of the 9.5-psi data from Table I, where the velocities are plotted versus their values of λ/D. This figure reveals that the wave velocity V_w is significantly larger than the droplet velocity and that both dip slightly as λ/D approaches π. The large error bars for the jet velocity prohibit any strong statements concerning the magnitude of V_j. It *appears* from these data that the jet velocity is comparable to the droplet velocity and is substantially less than the wave velocity; however, the error bars are relatively large and only more precise measurements of V_j would bear this out.

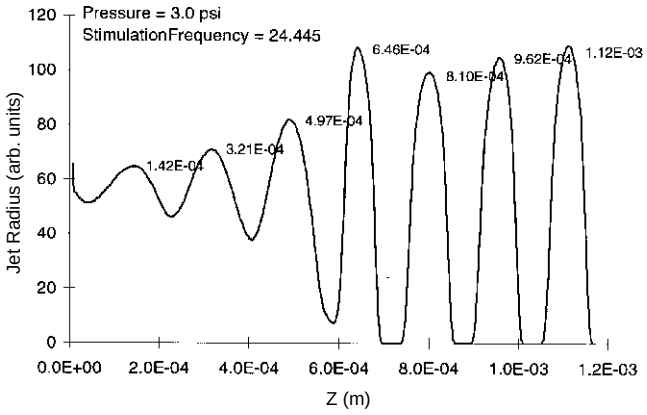

Figure 9. Surface profile of large initial disturbance jet.

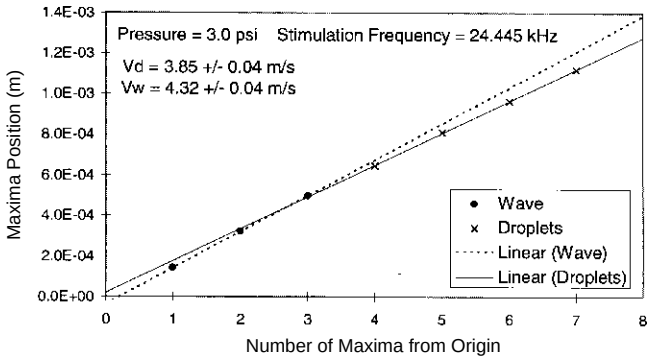

Figure 10. Wave maxima versus distance from origin: 3.0 psi.

Large-Amplitude Wave Propagation. The propagation of large-amplitude waves was studied by analyzing plots like that showin Fig. 9. The droplets, as represented in this plot, break away from the jet at about 7.0E – 04 m. Therefore, the maxima (minima) to the left of this point are on the continuous part of the stimulated jet, whereas the maxima to the right of 7.0E – 04 m are those of the droplets that have broken off. The numbers near the curve in the figure are the values for z where the jet radii are at local maxima. From these numbers, the wavelength of the disturbance on the jet and the droplet spacing can be determined.

In Fig. 10, the z values of the maxima discussed above are plotted in the sequence in which they occur for both the wave and droplets. The slopes of the fitted lines for each are the velocities for each: V_d = 3.85 ± 0.04 m/s and V_w = 4.32 ± 0.04 m/s. The difference between the droplet and wave velocities is thought to be due to a retarding force acting on the breakoff droplet during the last period for which the droplet is still connected to the jet.[3] However, this mechanism is probably inconsistent with the measurements of V_j and V_d compared in Fig. 8.

Figure 11 shows a similar plot for the maxima from a 9.5-psi large-amplitude stimulated jet. The wave velocity calculated by a linear fit of the wave maxima data gives V_w = 9.17 ± 0.23 m/s, which is close to the velocity droplet velocity of 9.00 ± 0.04 m/s. The large error for V_w calculated from the points in Fig. 11 is not all from random measurement error, but has a large contribution from the fact that the maxima are not linearly spaced along the length of the jet. As a comparision, the value for V_w with small-amplitude stimulation of 9.5-psi jets is 9.53 ± 0.06 m/s, obtained from the average of a large number of measurements.

A closer examination of the variable wavelength of the high-amplitude surface deformation is shown in Fig. 12.

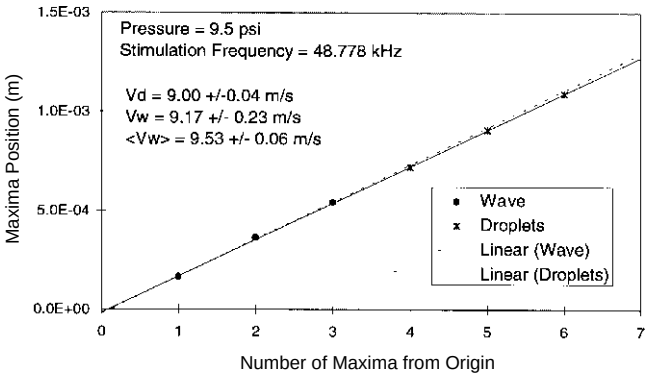

Figure 11. Wave maxima versus distance from origin: 9.5 psi

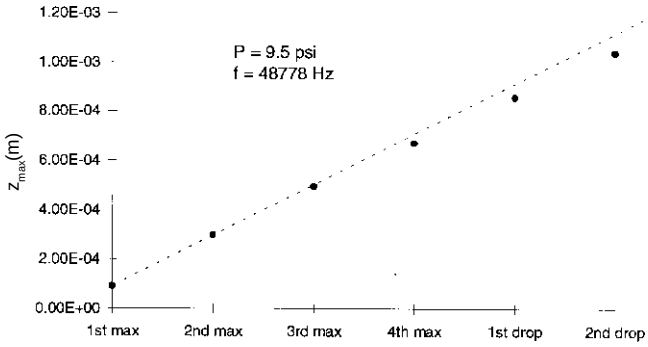

Figure 12. Position of maxima along jet.

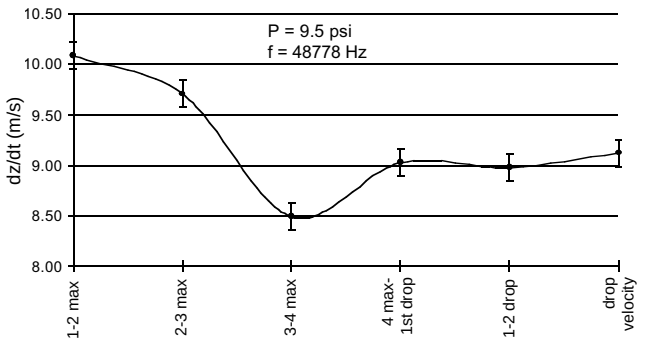

Figure 13. Wave velocity profile on highly stimulated jet for 9.5 psi.

This plot shows an expanded view of the wave maxima positions along the axis of the jet for the wave and the first two free droplets for P = 9.5 psi. The line in Fig. 12 is drawn connecting the first two points on the left and shows that the subsequent points fall successively farther below the line. Taking the differences between adjacent z_{max} values and dividing by the period of stimulation yields the velocity of the wave maxima (droplet) averaged over one $\lambda(L)$. A plot of these velocities for the 9.5-psi jet stimulated at 48.778 kHz is shown in Fig. 13. The effect of the variable wavelength of the wave on the local values of V_w is apparent in this figure, which shows that V_w dips sharply near the breakoff point and then appears to increase to the (constant) droplet velocity. Similar behavior is exhibited by the 3.0-psi, 24.445-kHz data plotted in Fig. 14. These data appear to indicate that the disturbance on the surface of the jet is slowing down as it approaches the breakoff point.

One implication of V_w not being constant along the length of the stimulated jet is that V_w is probably not equal to V_j. However, to say this with certainty would require knowledge

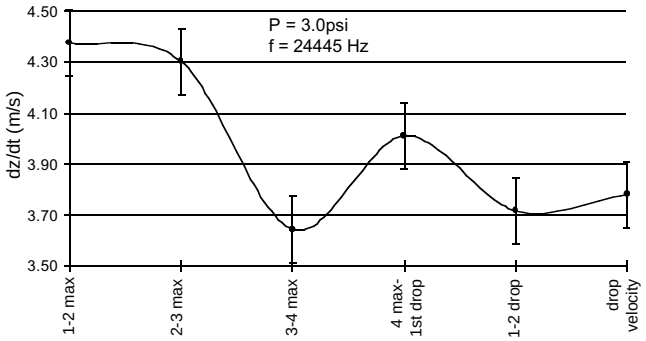

Figure 14. Wave velocity profile on highly stimulated jet for 3.0 psi.

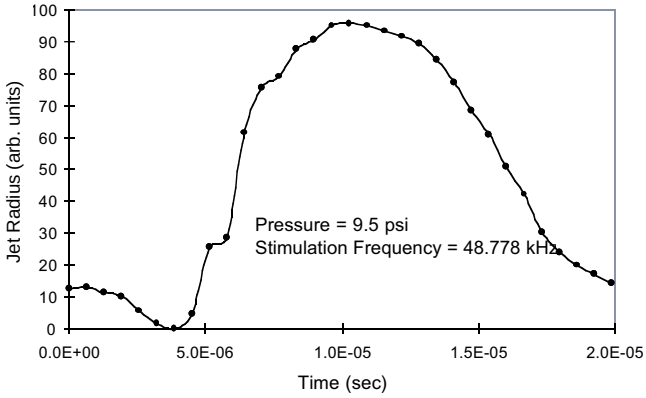

Figure 15. Stimulated jet radius versus time.

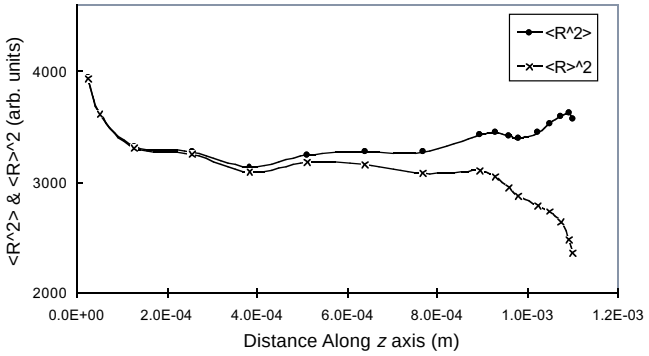

Figure 16. Plot of $\langle R^2 \rangle$ and $\langle R \rangle^2$ versus z.

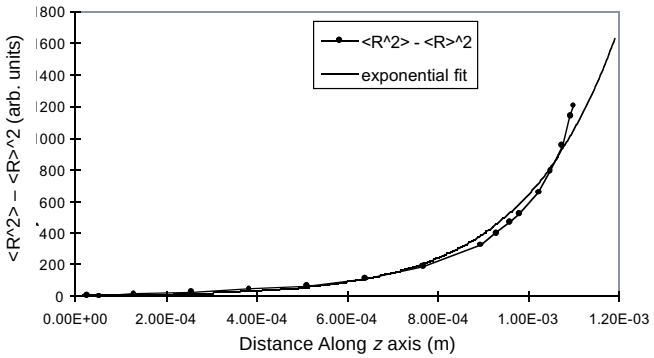

Figure 17. Plot of $\langle R^2 \rangle - \langle R \rangle^2$ versus z.

of the velocity of the fluid everywhere in the jet, as the surface deformations will be displacing the fluid below the surface of the jet, producing local variations in the z component of the fluid velocity. It is possible, though not likely, that the local value of V_j averaged over a radial cross section of the jet is equal to the velocity of the surface bounding the cross section. This is clearly not an issue with small-amplitude stimulation, where the surface deformations are too small to drive the interior fluid. An analogous situation would be that of shallow and deep water waves, where the magnitude of the surface deformation relative to the depth of the water has a large effect on the physics of the wave propagation.

The overall behavior of the wave and the breakoff process found here seems to be consistent with prior analyses in that there is an *apparent* reduction in the fluid momentum in the droplet breakoff region.[4] What has actually been determined experimentally here is that the surface wave velocity is retarded near breakoff, which is also the point where the amplitude of the stimulation becomes of the same order as the jet radius.

Large-Amplitude Wave Growth. The rate at which the perturbation on the surface of the jet grows was determined by Rayleigh to be an exponential function of time for $\lambda/D > \pi$. As discussed before, once the amplitude of the wave on the jet becomes too large for the conditions leading to the dispersion relation, Eq. 4, the simple theory probably does not describe the real physical situation as well.

In Fig. 15, the radius of the jet is measured as a function of time for one period at a fixed position along z. In this plot $R(t)$ is a periodic function, but not described by a single frequency component.[5]

It is of interest to calculate the square of the time averaged radius, $\langle R \rangle^2$, and of the square of the radius, $\langle R^2 \rangle$; for comparison purposes. If the jet velocity at a particular point along the axis of the jet is assumed to be constant with respect to time, then $\langle Q \rangle = \rho \pi V_j \langle R^2 \rangle$. The value of $\langle R^2 \rangle$ versus z is plotted in Fig. 16, along with the value of $\langle R \rangle^2$. At first glance, the data plotted in this figure appear to be quite noisy and, not unexpectedly, $\langle R^2 \rangle$ does not equal $\langle R \rangle^2$ everywhere. The values of $\langle R^2 \rangle$ and $\langle R \rangle^2$ are experimentally equal near the origin of the jet (the orifice plate), and they diverge as the jet moves away from the orifice. This divergence is presumably due to the meniscus formed on the surface of the plate surrounding the nozzle. For larger values of z, $\langle R^2 \rangle$ and $\langle R \rangle^2$ continue to diverge, with the difference becoming greatest at the breakoff point.

It is surprising though, that the difference $\langle R^2 \rangle - \langle R \rangle^2$ plotted versus z (see Fig. 17) results in a curve that is quite smooth and is reasonably well described by a simple exponential function. The smoothness of this curve indicates that the variations between the $\langle R^2 \rangle$ and $\langle R \rangle^2$ data are real and not noise. The difference data also show that the amplitude disturbance grows with time in an exponential fashion, as predicted by Rayleigh.[1] If the time-dependent radius can be written as $R(t) = R_0 + r(t)$, where $r(t)$ is a periodic function of time and $\langle r \rangle = 0$, then $\langle R^2 \rangle - \langle R \rangle^2 = \langle r^2 \rangle$. If $r(t) = r_0 \cos(\omega t)$, then $\langle r^2 \rangle = r_0^2/2$, and the amplitude, r_0, is found to grow exponentially with time.

Conclusions

The analysis of waves on a cylindrical jet yields a straightforward analytical solution only when the amplitude of the deformation is small. Small deformation waves were generated for $\lambda/D < \pi$ and the phase velocity of these waves as a function of λ/D was found to be in good agreement with the dispersion relation, Eq. 4. This dispersion relation came from the solution of Eq. 3 with many simplifying assumptions and approximations. When these conditions are not allowed, as is the case when the amplitude of the wave motion becomes large, the solutions become less useful in describing the actual wave motion of the jet.

The deviation from simple theory of the wave when the surface deformation is large was revealed in the measurements of the wave propagation along the length of the jet for $\lambda/D > \pi$. We found that the wavelength of the large-amplitude deformation decreased as the amplitude increased in the direction of the jet velocity. This suggests that (1) the jet and wave velocities are probably not the same, as is often assumed, and (2) the wave velocity decreases as the amplitude of the wave increases, until droplet breakoff occurs.

The droplet velocity was shown, without question, to be less than the wave velocity. Schneider[3] and Lienhard[4] considered the problem and found that the droplet velocity should be less than the jet velocity due to surface tension effects during the period just before breakoff. In both cases, however, it was assumed in the analyses that the jet velocity and wave velocity were the same when $\lambda/D > \pi$. It appears from the measurements made here that this is unlikely. It would not be surprising to find the nonlinear nature of the fluid dynamics to be important when the amplitudes of the surface deformations are no longer small.

Measurements of the jet radius, R, as a function of time at constant z showed that the radial motion of the surface of the jet is not simple periodic motion.[5] The time-averaged values of R^2 and R were used to show that the growth of the deformation amplitude is still roughly an exponential function of time, when the amplitude is defined as $r_0^2 = [\langle R^2\rangle - \langle R\rangle^2]$, even though there is a more complicated dependence of the individual values of $\langle R^2\rangle$ and $\langle R\rangle^2$ on z.

An experimental difficulty that proved to be nontrivial was the dependence of the jet radius on jet velocity. This relationship makes the measurement of jet velocity somewhat more complicated and requires an extremely accurate measurement of the jet radius in order to maintain a reasonable error for V_j. Even with the high-resolution video system measurements, where the radius measurement errors were quite small, the jet velocity measurement could still not be made routinely with an error of less than a few percent, which is large compared with the errors associated with the droplet and wave velocity measurements. More accurate measurements of the jet velocity will be needed before comparison of the wave and jet velocities can be made with more confidence.

References

1. Lord Rayleigh, *Proc. Roy. Soc.*, **29** 71 (1879).
2. R. Fagerquist, *Proceedings IS&T's 7th International Congress on Advances in Non-Impact Printing Technologies*, pp. 67–75 (1991).
3. J. Schneider, Internal Memo, Scitex Digital Printing, Inc., July 1992.
4. J. H. Lienhard, *J. Fluids Eng.*, **106**: pp. 13-17 (1984).
5. A. Soucemarianadin, J. Xing, P. Attane and A. Dunand, *Proceedings IS&T's 7th International Congress on Advances in Non-Impact Printing Technologies*, October 1991, pp. 367-375.